Nonequilibrium Particle and Continuum Analyses of Stardust Entry for Near–Continuum Conditions

Iain D. Boyd*

University of Michigan, Ann Arbor, Michigan, 48109-2140, USA

Kerry Trumble[†]

Eloret Corporation, Sunnyvale, California, 94086, USA

Michael J. Wright[‡]

NASA Ames Research Center, Moffett Field, California, 94035-1000, USA

The Stardust Sample Return Capsule (SRC) entered the Earth's atmosphere at a velocity of 12.6 km/s. At high altitude, the flow field is expected to be in a strong state of thermochemical nonequilibrium. In the present study, both continuum (CFD) and particle (DSMC) methods are used to analyze the forebody flow of the SRC at an altitude of 81 km where the freestream Knudsen number is about 0.005. The very large entry velocity represents a highly energetic condition for which the thermochemistry models are not well calibrated. Direct comparisons between baseline CFD and DSMC models give enormous differences in basic flow field properties. To study the discrepancy between the solutions, different methods for determining the temperature used by CFD to control the dissociation and ionization reactions are investigated. Also, a new model is introduced for the DSMC technique that makes it possible to simulate reverse direction chemical reactions in a manner more consistent with that used in CFD. While the revised CFD and DSMC results are in better agreement with each other, under these highly-energetic, near-continuum flow conditions, significant differences remain between continuum and particle solutions. Additional CFD computations performed at lower altitude indicate, as expected, that flow field results become less sensitive to details of the chemistry modeling further into the continuum regime.

I.   Introduction

The Stardust payload was launched in February 1999 on a mission to use aerogel to collect samples of material from comet Wild-2. In January 2006, almost exactly seven years later, after collecting the cometary dust and returning to Earth, the Stardust Sample Return Capsule (SRC) entered the atmosphere at a velocity of 12.6 km/s. This is the highest energy vehicle entry ever undertaken. Shortly after entering the atmosphere, the Stardust SRC landed in Utah allowing its precious scientific payload to be safely recovered.

The forebody thermal protection material used on Stardust was PICA (Phenolic Impregnated Carbon Ablator) that has also been selected as a candidate material for use on NASA's Orion Crew Exploration Vehicle (CEV). The combination of having an entry velocity similar to Mars return, and the use of PICA as heat shield material make it of significant interest to perform detailed analyses of the Stardust SRC entry even after the successful completion of its mission.

A number of studies of the aerothermodynamics of the Stardust SRC were performed prior to the mission.[1–4] These studies conducted flow field analyses using both continuum CFD methods (by solving the Navier-Stokes equations) and particle methods (using the direct simulation Monte Carlo method, DSMC[5]).

---

*Professor, Department of Aerospace Engineering, 1320 Beal Ave, AIAA Associate Fellow.

[†]Research Scientist, Reacting Flow Environments Branch, AIAA Member.

[‡]Senior Research Scientist, Reacting Flow Environments Branch, Mail Stop 230-2, AIAA Senior Member.

However, the DSMC study[3] was focused on the high-altitude aerodynamics of the capsule and did not include the effects of ionization reactions. A more recent study compared CFD and DSMC simulation results for Stardust at 80 km.[6]

The primary goal of this study is to perform high-altitude analyses of the aerothermodynamic environment on the forebody of the Stardust SRC. Computations are performed with both continuum and particle methods. Direct comparisons between the solutions provided by these techniques allows evaluation of differences between these approaches for modeling the strongly nonequilibrium thermochemical phenomena generated under highly energetic entry conditions. Comparisons in this environment are also needed to aid in further development of CFD-DSMC hybrid methods[7] to be extended to flows involving thermochemical nonequilibrium.

The geometry of the Stardust SRC and the entry conditions chosen for study are first described. The two numerical methods employed in the study are described in some detail. These consist of a CFD code for solving the Navier-Stokes equations with coupled nonequilibrium thermochemistry, and a DSMC code that also includes thermochemical nonequilibrium. Emphasis is given on any differences in the ways in which the important thermochemical nonequilibrium processes are simulated. Results are then presented in which direct comparisons are made between several sets of continuum and particle simulations. The results are discussed and final conclusions formulated.

II.   Flow Conditions

The geometry of the Stardust SRC is shown schematically in Fig. 1. The forebody consists of a 60-deg. half-angle, spherically blunted cone with a nose radius of 0.2202 m. In the computations, a small portion of the shoulder is included that has a radius of 0.02 m. Most of the computations consider the Stardust SRC entry trajectory point at an altitude of 81 km where the freestream Knudsen number is about 0.005 based on the diameter of the capsule. At this point, the velocity is 12,385 m/s, the mass density is 1.269×10^{-5} kg/m^3, and the temperature is 217.6 K. This Knudsen number is in a region where relatively small differences between continuum and particle simulation results for hypersonic flow are expected. For example, in comparing Mach 25 flow of non-reacting argon over a cylinder, differences in predicted peak heating between continuum and particle simulations were about 5% at a Knudsen number of 0.01 and about 2% at Kn=0.002.[8] The 81 km trajectory point is also of interest due to the availability of radiation measurements taken during the Stardust SRC entry that are not yet published.

III.   Numerical Methods

The two different numerical approaches applied in this study are: (1) CFD solution of the continuum Navier-Stokes equations using the DPLR code; and (2) particle-based DSMC computation. In each case, an 11-species, 19-reaction, thermochemical nonequilibrium approach is adopted. The wall temperature is assumed fixed at a temperature of 2,000 K. The wall material PICA is assumed to be fully catalytic to ions (that recombine into their neutral atoms and molecules) and atoms (that recombine into molecules). Ablation processes are not included in these studies.

III.A.   Details of the Continuum Flow Model

The continuum computations are performed using the DPLR CFD code.[9, 10] DPLR is a parallel multiblock finite-volume code that solves the Navier-Stokes equations including finite-rate chemistry and the effects of thermal nonequilibrium. The Euler fluxes are computed using a modified (low-dissipation) form of Steger-Warming flux vector splitting,[11] with third-order spatial accuracy obtained via MUSCL extrapolation.[12] Viscous fluxes are computed to second-order accuracy using a central difference approach. DPLR has been used previously on several other planetary entry simulations.[9, 13, 14]

The flow is assumed to be in a state of thermochemical nonequilibrium with three separate temperatures for the translational, rotational, and vibrational modes. Viscous transport and thermal conductivity are modeled using the mixing rules presented by Gupta et al.[15] which have been shown to be reasonable approximations of the more accurate Chapman-Enskog relations in this flow regime.[16, 17] The bifurcation method is used to compute the species diffusion coefficients.[18] This method allows for the variations in species diffusion coefficients to be accurately modeled without sacrificing the requirement that the diffusion

American Institute of Aeronautics and Astronautics

velocities sum identically to zero.

Rotational relaxation is modeled using the relaxation time based on the Parker model.[19] Vibrational relaxation is modeled using a Landau-Teller formulation, where relaxation times are obtained from Millikan and White,[20] assuming simple harmonic oscillators, with the high-temperature correction of Park.[21] The baseline 19-reaction finite-rate air chemistry model uses the rates[22,23] that are listed in Table I. The backward rates are computed using the forward rates and equilibrium constants evaluated using the van't Hoff equation. Dissociation reaction rates are computed according to the two-temperature model of Park.[21]

Surface catalysis is modeled using a diffusion limited approach.[21] The surface is assumed to be fully catalytic to N_2 and O_2 recombination, which should be reasonable for the PICA TPS material based on its expected similarity to graphite TPS systems.

III.B. Details of the Particle Flow Model

The particle computations employ a DSMC code developed specifically for hypersonic, ionized flow simulations.[24] Models are implemented for rotational[25] and vibrational[26] energy exchange that are consistent with those employed in DPLR. Most of the chemical reactions are simulated using the Total Collision Energy (TCE) model except for the dissociation of nitrogen and oxygen. These reactions employ the Vibrationally Favored Dissociation (VFD) model.[27] The VFD model makes it possible to bias the dissociation reaction probability in favor of molecules that possess a higher vibrational energy. In this way, the important phenomenon of vibration–dissociation coupling can be simulated. In the present work, the VFD favoring parameter ϕ is set to 2.0 for nitrogen dissociation and 0.5 for oxygen dissociation, as determined in prior work.[27] A recent detailed DSMC study of nitrogen dissociation suggests that the VFD model with $\phi=2$ emulates the behavior of a more sophisticated approach.[28]

The baseline set of chemical reactions and rate coefficients employed in the DSMC computations are listed in Table II. All of the forward rates are the same as those employed in DPLR except for the two direct ionization reactions:

$$N + E^- \rightarrow N^+ + 2E^- \tag{1}$$

$$O + E^- \rightarrow O^+ + 2E^- \tag{2}$$

It is not possible to employ the low, negative temperature exponents of the rates employed by DPLR in the DSMC TCE chemistry model. The rates employed by DSMC are those reported by Wilson.[30] The lower activation energies in these rates are based on the premise that most atomic ionization occurs not from the ground electronic state, but rather from the lowest excited states of nitrogen and oxygen. These rates are also employed in some DPLR computations. The Park[22] and Wilson[30] ionization rates for both nitrogen and oxygen are compared in Fig. 2 as a function of temperature.

The presence of electrons in the flow field presents a challenge for the DSMC technique due to their very small mass and associated very high thermal velocities. Under the assumption of ambi-polar diffusion in which the diffusion rates of electrons and ions are assumed equal, the standard approach in DSMC for handling this situation is to tie each electron particle to the ion particle with which it was created in the ionization process.[31] In the present highly energetic flow condition, the ionization degree is expected to be significant and keeping track of pairs of electrons and ions can cause difficulties for the standard DSMC approach. Therefore, a model previously developed for DSMC computation of plasma thrusters[32] is employed here. In this approach, the average ion velocity in each computational cell is evaluated and all electrons in each cell are moved with this average velocity. While the approach does not guarantee charge neutrality, in practice it is found that neutrality is achieved everywhere in the flow domain within a few percent. This approach for handling electrons is significantly more robust than the standard DSMC approach.

III.C. DSMC Backward Rate Modeling

As explained above, the standard continuum approach for computing the backward rate of a chemical reaction uses:

$$k_b(T) = \frac{k_f(T)}{K_e(T)} \tag{3}$$

where k_f and k_b are the forward and backward reaction rates, K_e is the equilibrium constant, and T is temperature. The DSMC TCE chemistry model requires that reaction rate coefficients in both the forward and backward directions be specified in modified Arrhenius form; for example:

American Institute of Aeronautics and Astronautics

$$k_i = a_i T^{\eta_i} exp(-\theta_i/T) \tag{4}$$

where θ_i is the activation temperature of the reaction. The restriction on the TCE model to use Eq. (4) presents a difficulty in trying to ensure that consistent rates are used in the DSMC and DPLR simulations since the equilibrium constants, K_e, are not simple functions of temperature. The standard approach taken in DSMC is to fit the backward rate coefficients over a "reasonable" temperature range to a modified Arrhenius form. The backward rate coefficients provided in Table II were obtained in this way for temperatures in the range of 5,000 to 20,000 K.[24] For some reactions, this approach is unsatisfactory even over a limited temperature range. In addition, the Stardust entry conditions of interest here will generate temperatures far in excess of 20,000 K requiring new fits for all backward rate coefficients to be evaluated. These problems are illustrated in Fig. 3 where the backward rates coefficients for the Zeldovich exchange reactions (reactions 4 and 5 in Tables I and II) are shown as a function of temperature. The lines labeled "Exact" are obtained using the accurate equilibrium constant employed by DPLR along with the forward rate coefficients listed in Table I. The lines labeled "Arrhenius" are those listed in Table II that are found to agree with the "Exact" values at temperatures of 5,000 and 20,000 K. However, at larger temperatures, particularly for reaction 4, there are orders of magnitude difference between the reaction rates employed in DSMC and DPLR.

To address these issues, a new DSMC model for simulating backward rates is developed that represents a simple extension of the TCE model. In the new approach, the backward rate coefficient is written as:

$$k_b(T) = \frac{k_f(T)}{exp(-\theta_f/T)} \frac{exp(-\theta_f/T)}{K_e(T)} = a_f T^{\eta_f} \frac{exp(-\theta_f/T)}{K_e(T)} \tag{5}$$

In the DSMC implementation of this model, the quotient term on the far right hand side is evaluated by computing the translational temperature in each cell of the computational domain. The leading term on the right hand side is evaluated using the standard TCE model where the activation temperature is zero. For all reactions, the temperature-dependent form of the equilibrium constant used in DSMC is identical to that employed by DPLR. Figures 3 and 4 show evaluations of the average backward rate coefficients obtained using the new model in heat bath, equilibrium DSMC calculations. Clearly, the new model is able to accurately simulate the backward rates employed in the continuum approach, and these rates are in some cases orders of magnitude different from the rates listed in Table II used previously in DSMC computations. Note that, for the associative ionization reactions shown in Fig. 4, in some cases the new model gives faster rates and in some cases lower rates.

IV.   Flowfield Results

The meshes used in the DPLR computations consist of three blocks containing 24x128, 64x128, and 48x128 cells. In each case, the mesh is grown out hyperbolically from the vehicle surface to ensure orthogonality and then adapted to contours of Mach number.

The DSMC computations employ a single mesh containing 100 by 200 cells in which the cell dimension in the flow direction is everywhere less than the local mean free path. Typically, about two million particles are employed of which 40,000 are electrons. The timestep used in the DSMC computations is smaller than the mean free time anywhere in the flow field.

IV.A.   Comparison of Baseline Cases

Comparison is first made of solutions obtained with DPLR and DSMC using the baseline set of rate coefficients. Figure 5 provides a comparison of the translational temperature contours. Qualitatively, this comparison shows: (1) the shock wave predicted by DSMC is significantly thicker than that simulated by DPLR; and (2) the peak translational temperature from DSMC is significantly higher than that simulated by DPLR.

Quantitative differences between the simulation results can be assessed using Fig. 6 that shows temperature profiles along the stagnation streamline. In all comparisons, the solid lines represent the baseline DSMC results and the dashed lines are the baseline DPLR results. These profiles show enormous differences between the DSMC and DPLR solutions that were not anticipated based on prior non-reacting CFD/DSMC comparisons at Mach 25.[8] DSMC predicts a peak translational temperature that is more than a factor of two higher than the DPLR result. The DSMC predictions for peak rotational and vibrational temperatures

are also higher than the DPLR solutions. Note that DSMC provides the translational temperature of the electrons whereas DPLR assumes that the electrons have the same translational temperature as the bulk gas. The DSMC profile of electron temperature lies between the rotational and vibrational temperature profiles.

Profiles of the number densities of the neutral species are shown in Fig. 7. The DPLR solutions generally show a more compact shock structure and a higher level of dissociation in comparison to the DSMC results. Due to the use of the same fully catalytic surface boundary condition in each simulation, the species concentrations at the wall are in good agreement. Profiles of the number densities of the ions and electrons are shown in Fig. 8. Here there is very little agreement of any kind between the two solutions. DPLR predicts a peak electron number density that is about a factor of 8 higher than the DSMC peak prediction. Most of the DPLR ion number density stems from atoms whereas the DSMC results contain a significant population of N_2^+.

Profiles of the vehicle surface pressure and heat flux are compared in Fig. 9. As expected, the profiles of pressure are in very good agreement. There is about a 13% difference in peak heating with DSMC predicting a lower value. Given the significant differences in flow field profiles, this level of agreement is perhaps surprising. The explanation lies in the use of the fully catalytic surface boundary condition in both simulations.

The very significant differences in flow field properties obtained between the DPLR and DSMC results are most likely caused by differences in the treatment of chemistry. In the following sections, results from additional DPLR and DSMC computations are presented in which the goal is to try and close gaps existing in the models used to generate the baseline solutions.

IV.B.   Effects of Continuum Chemistry Modeling

The baseline DPLR case employed the rates in Table I, the standard Park two-temperature model for dissociation in which the controlling temperature $T = T_t^{0.5} \times T_v^{0.5}$, and all other reactions are controlled solely by the translational temperature. To try to understand the source of the differences between the DPLR and DSMC solutions, several further DPLR simulations are performed in which the approach to chemistry modeling is varied. Effects investigated include use of the Wilson[30] direct ionization rates.

Another issue studied considers use of different controlling temperatures $T = T_t^n \times T_v^{1-n}$ for both dissociation and ionization reactions. For dissociation, heat bath studies indicate that nonequilibrium DSMC dissociation rates are closer to those obtained in DPLR with n=0.3 rather than the baseline of n=0.5. For direct ionization, in DSMC the collision energy is determined by the relative velocity between the atom and the electron that is generally dominated by the electron velocity. Thus, DSMC simulation of direct ionization is more closely approximated in DPLR using n=0.0 assuming that the vibrational temperature in DPLR is a better approximation to the electron temperature than the translational temperature.

The effects of some of these changes on the electron number density along the stagnation streamline can be seen in Fig. 10. There is a decrease in peak electron number density of a factor of 30 when the temperature controlling the direct ionization reaction is changed from the translational value to the vibrational value. By comparison, there is essentially no difference in the electron number density when switching from the Park to the Wilson rates.

The baseline DPLR simulation results are compared with the modified chemistry DPLR profiles for stagnation streamline temperatures in Fig. 11. In these comparisons, the modified chemistry profiles are shown as dash–dot–dash lines. The changes in the controlling temperatures for dissociation and direct ionization lead to significant increases in the peak temperatures for each of the translational, rotational, and vibrational modes. In addition, the shock thickness is significantly increased. All of these changes are qualitatively in better agreement with the DSMC results.

Profiles of the number densities of the neutral species are shown in Fig. 12. There are important differences in the profiles between these two DPLR solutions with the modified chemistry modeling leading to a more diffuse shock. The simulations show very good agreement at the surface due to the fully catalytic boundary condition. Profiles of the number densities of the ions and electrons are shown in Fig. 13. The modified chemistry modeling leads to a reduction by a factor of 30 in the peak electron number density. This is achieved through significant decreases in the rates of direct ionization. In addition, the number densities of the molecular ions are increased with the modified chemistry modeling. Again, all of these changes are in qualitative agreement with the DSMC baseline results.

Profiles along the vehicle surface of pressure and heat flux are compared in Fig. 14. Again, the pressure profiles are insensitive to the chemistry models. The modified DPLR chemistry modeling leads to a 20%

American Institute of Aeronautics and Astronautics

increase in peak heating. The increase is caused by an increase in temperature gradient at the surface in the modified chemistry case that is a result of the decreased level of ionization.

IV.C. Effects of Particle Modeling of Backward Reactions

The baseline DSMC case employed the best-fit modified Arrhenius rate coefficients listed in Table II for the backward reactions. To achieve better correspondence to the DPLR simulations, the new backward reaction DSMC chemistry model is applied to all reactions. This DSMC simulation employs all the forward rates listed in Table II along with the same equilibrium constants employed by DPLR.

The baseline DSMC simulation results are compared with the modified backward chemistry DSMC profiles for stagnation streamline temperatures in Fig. 15. In these comparisons, the modified chemistry DSMC profiles are shown as dash-dot-dot-dash lines. Clearly, there is very little difference in the temperatures due to the changes in chemistry modeling. Profiles of the number densities of the non-charged species are shown in Fig. 16. With the new backward chemistry model, there is clearly more nitric oxide. Due to the complex chemical mechanism, it is difficult to pinpoint an explanation for the differences. However, the increased level of nitric oxide is consistent with the significantly reduced backward rate for reaction 5 that depletes NO.

Stagnation streamline profiles of the number densities of the ions and electrons are shown in Fig. 17. More significant differences are found for these profiles. With the modified backward reaction model, the peak electron number density is reduced by a factor of three. The ions are now mostly atomic. The ion number densities of molecular nitrogen, oxygen, and nitric oxide computed with the modified model are more than an order of magnitude smaller than the baseline DSMC result. The decreases in N_2^+ and NO^+ are consistent with the revised backward rate coefficients shown in Fig. 4. The decreased levels of O_2^+ are traced to changes in the revised backward rates for Reactions 13 and 19.

The profiles of the vehicle surface pressure and heat flux are found to be essentially identical for the two DSMC cases.

For completeness, the modified DPLR and modified DSMC profiles are compared in Fig. 18 for temperature along the stagnation streamline. While the DSMC profiles are still much more diffuse, the level of agreement between DSMC and DPLR is much improved from the results shown in Fig. 6. Profiles of the number densities of the non-charged species along the stagnation streamline are shown in Fig. 19. While DPLR predicts strong levels of dissociation of oxygen and nitric oxide, in general the DSMC and DPLR profiles are in quite good agreement. Stagnation streamline profiles of the number densities of the ions and electrons are shown in Fig. 20. Although the peak electron number density predicted by the two methods is about the same, there are detailed differences in most of the ion profiles.

Profiles along the vehicle surface of pressure and heat flux are compared in Fig. 21. The pressures predicted by DSMC and DPLR remain in good agreement while there is now a very significant difference in peak heat flux with DPLR predicting a value that is about 40% higher.

IV.D. Effect of Knudsen Number

A final study is performed with DPLR at a lower altitude of 71 km to assess the effects of chemistry modeling for a condition that is further into the continuum regime. At this altitude, the freestream velocity is 12,063 m/s and the freestream Knudsen number is about 0.001. DPLR simulations are performed with the baseline chemistry model and with a case where dissociation is controlled using $n=0.3$, ionization is controlled using $n=0.0$, and the Wilson ionization rates are employed. Profiles of temperatures along the stagnation streamline are compared in Fig. 22 where the revised chemistry modeling results are shown as solid lines. In qualitative agreement with the profiles shown in Fig. 11, the revised chemistry modeling leads to significant increases in the peak temperature of all three energy modes and the shock becomes thicker.

Profiles of neutral species number densities along the stagnation streamline are shown in Fig. 23. The shock standoff distance is increased with the revised chemistry modeling, but in the post shock region as the boundary layer is entered, the two simulations are almost identical. The number density profiles of the charged species shown in Fig. 24 show similar qualitative behavior. Unlike the corresponding profiles shown for 81 km in Fig. 13, the peak levels of electron number density are now independent of the chemistry modeling as would be expected for the more continuum flow condition.

For completeness, the profiles of surface pressure and heat flux are shown in Fig. 25 and indicate independence from the chemistry modeling. In the 81 km case, the flow is so strongly nonequilibrium that

thermochemical nonequilibrium effects persist in the boundary layer. Here, at 71 km, the nonequilibrium effects are present in the shock region, but in the boundary layer the results are independent of the chemistry modeling.

V.   Conclusions

The return trajectory of the Stardust Sample Return Capsule generated the most energetic entry flight condition of a man-made vehicle. The energetic flow condition challenges computational modeling of the flow field as the existing thermochemical models for continuum and particle methods have not been calibrated in this highly energetic regime. The present study applied existing CFD (DPLR) and DSMC codes to the Stardust trajectory point at 81 km where the Knudsen number of 0.005 placed the flow in the near–continuum regime.

Comparisons of baseline DPLR and DSMC solutions showed enormous differences in basic flow field properties of temperatures and species number densities. For example, the peak translational temperature predicted by DSMC was more than a factor of two larger than that predicted by DPLR. Two subsequent studies were conducted to try to understand the differences in the solutions. First, the methods used by DPLR to determine the controlling temperature in the dissociation and direct ionization reactions were varied. For dissociation, more weight was given to the vibrational temperature, and for ionization, the vibrational temperature was fully used. Each of these approaches brought the DPLR approach more in line with that employed by DSMC. Second, a new DSMC model was introduced for simulating the backward rates of chemical reactions that makes it possible to employ the exact same backward rates as used by DPLR.

Each of the revisions to the numerical methods produced significant changes in the computed flow field properties. Comparison of the revised solutions produced a significant improvement in agreement between the DPLR and DSMC solutions for temperatures and number densities. However, fairly significant differences still existed leading to the conclusion that further investigation of the performance of thermochemistry models used by continuum and particle methods is required under near-continuum and highly energetic flow conditions. Comparisons of such solutions with detailed experimental measurements is required in order to assess the accuracy of the various models.

The continuum approach was also applied to the Stardust trajectory point at 71 km altitude, where the Knudsen number is 0.001. At this more continuum condition, there remained significant sensitivity of the computed properties in the shock region to details of the chemistry modeling. However, the overall levels of dissociation and ionization, as well as surface heat flux, were not significantly changed through use of the different chemistry models.

VI.   Future Work

The original goal of this study was to provide flow field simulation results that can be used to compute radiation spectra to be compared with measurements conducted during the Stardust SRC entry. One of the next steps beyond the current investigation is to assess any sensitivity observed in chemistry modeling on the resulting radiative spectra. Comparison with the spectra measured during Stardust entry may help to determine preferred approaches for chemistry modeling in both continuum and particle methods.

The results of the current study also demonstrate a need to step back and perform a careful series of comparisons between continuum and particle methods for the types of conditions experienced by Stardust. Specifically, it is needed to determine which physical mechanisms contribute most to the differences observed in the DSMC and CFD results.

VII.   Acknowledgments

References

[1]Olynick, D., Chen, Y.-K., and Tauber, M. E., "Aerothermodynamics of the Stardust Sample Return Capsule," *Journal of Spacecraft and Rockets*, Vol. 36, 1999, pp. 442-462.

[2]Mitcheltree, R. A., Wilmoth, R. G., Cheatwood, F. M., Brauckmann, G. J., and Greene, F. A., "Aerodynamics of Stardust Sample Return Capsule," *Journal of Spacecraft and Rockets*, Vol. 36, 1999, pp. 429-435.

[3]Wilmoth, R. G., Mitcheltree, R. A., and Moss, J. N., "Low-Density Aerodynamics of the Stardust Sample Return Capsule," *Journal of Spacecraft and Rockets*, Vol. 36, 1999, pp. 436-441.

[4]Gupta, R. N., "Aerothermodynamic Analysis of Stardust Sample Return Capsule With Coupled Radiation and Ablation," *Journal of Spacecraft and Rockets*, Vol. 37, 2000, pp. 507-514.

[5]Bird, G. A., *Molecular Gas Dynamics and the Direct Simulation of Gas Flows* Oxford University Press, Oxford, 1994.

[6]Ozawa, T., Zhong, J., Levin, D. A., Boger, D., and Wright, M. J., "Modeling of the Stardust Renetry Flows With Ionization in DSMC," AIAA Paper 2007-0611, January 2007.

[7]Schwartzentruber, T. E., Scalabrin, L. C., and Boyd, I. D., "A Modular Particle-Continuum Method for Hypersonic Non-equilibrium Gas Flows," *Journal of Computational Physics*, Vol. 216, 2007, pp. xxx-yyy.

[8]Lofthouse, A. J., Scalabrin, L. C., and Boyd, I. D., "Continuum Breakdown, Velocity Slip and Temperature Jump in Hypersonic Aerothermodynamics," AIAA Paper 2007-0208, January 2007.

[9]Wright, M., Loomis, M., and Papadopoulos, P., "Aerothermal Analysis of the Project Fire II Afterbody Flow," *Journal of Thermophysics and Heat Transfer*, Vol. 17, No. 2, 2003, pp. 240-249.

[10]Wright, M., Candler, G., and Bose, D., "Data-Parallel Line Relaxation Method for the Navier-Stokes Equations," *AIAA Journal*, Vol. 36, No. 9, 1998, pp. 1603-1609.

[11]MacCormack, R. and Candler, G., "The Solution of the Navier-Stokes Equations Using Gauss-Seidel Line Relaxation," *Computers and Fluids*, Vol. 17, No. 1, 1989, pp. 135-150.

[12]Yee, H., "A Class of High-Resolution Explicit and Implicit Shock Capturing Methods," NASA TM 101088, Feb. 1989.

[13]Wercinski, P., Chen, Y.-K., Loomis, M., Tauber, M., McDaniel, R., Wright, M., Papadopoulos, P., Allen, G., and Yang, L., "Neptune Aerocapture Entry Vehicle Preliminary Design," AIAA Paper No. 2002-4812, Aug. 2002.

[14]Wright, M., Bose, D., and Olejniczak, J., "The Impact of Flowfield Radiation Coupling on Aeroheating for Titan Aerocapture," *Journal of Thermophysics and Heat Transfer*, Vol. 19, No. 1, 2005, pp. 17-27.

[15]Gupta, R., Yos, J., Thompson, R., and Lee, K., "A Review of Reaction Rates and Thermodynamic and Transport Properties for an 11-Species Air Model for Chemical and Thermal Nonequilibrium Calculations to 30000 K," NASA RP-1232, Aug. 1990.

[16]Palmer, G. E. and Wright, M. J., "A Comparison of Methods to Compute High Temperature Gas Viscosity," *Journal of Thermophysics and Heat Transfer*, Vol. 17, No. 2, 2003, pp. 232-239.

[17]Palmer, G. E. and Wright, M. J., "A Comparison of Methods to Compute High Temperature Gas Thermal Conductivity," AIAA Paper No. 2003-3913, Jun. 2003.

[18]Bartlett, E. P., Kendal, R. M., and Rindal, R. A., "An Analysis of the Coupled Chemically Reacting Boundary Layer and Charring Ablator: Part IV - A Unified Approximation for Mixture Transport Properties for Multicomponent Boundary-Layer Applications," NASA CR-1063, June 1968.

[19]Parker, J. G., "Rotational and Vibrational Relaxation in Diatomic Gases," *Physics of Fluids*, Vol. 2, 1959, pp. 449-462.

[20]Millikan, R. and White, D., "Systematics of Vibrational Relaxation," *Journal of Chemical Physics*, Vol. 39, No. 12, 1963, pp. 3209-3213.

[21]Park, C., *Nonequilibrium Hypersonic Aerothermodynamics*, Wiley, New York, 1990.

[22]Park, C., "Review of Chemical-Kinetic Problems of Future NASA Missions, I: Earth Entries", *Journal of Thermophysics and Heat Transfer*, Vol. 7, No. 3, 1993, pp. 385-398.

[23]Bose D. and Candler, G., "Thermal Rate Constants of the N2 + O =ED NO + N Reaction Using Ab Initio 3A" and 3A' Potential Energy Surfaces," *Journal of Chemical Physics*, Vol. 104, No. 8, 1996, pp. 2825-2833.

[24]Boyd, I. D. and Gokcen, T., "Computation of Axisymmetric and Ionized Hypersonic Flows Using Particle and Continuum Method," *AIAA Journal*, Vol. 32, 1994, pp. 1828-1837.

[25]Boyd, I. D., "Analysis of Rotational Nonequilibrium in Standing Shock Waves of Nitrogen," *AIAA Journal* Vol. 28, 1990, pp. 1997-1999.

[26]Boyd, I. D., "Analysis of Vibrational-Translational Energy Transfer Using the Direct Simulation Monte Carlo Method," *Physics of Fluids A*, Vol. 3, 1991, pp. 1785-1791.

[27]Haas, B. L. and Boyd, I. D., "Models for Direct Monte Carlo Simulation of Coupled Vibration-Dissociation," *Physics of Fluids A*, Vol. 5, 1993, pp. 478-489.

[28]Bondar, Y. and Ivanov, M., "DSMC Dissociation Model Based on Two-Temperature Chemical Rate Constant," AIAA Paper 2007-0614, January 2007.

[29]Boyd, I. D., "Modeling of Plasma Formation in Rarefied Hypersonic Entry Flows," AIAA Paper 2007-0206, January 2007.

[30]Wilson, J., "Ionization Rate of Air Behind High-Speed Shock Waves," *Physics of Fluids*, Vol. 9, 1966, pp. 1913-1921.

[31]Bird, G. A., "Nonequilibrium Radiation During Re-entry at 10 km/s," AIAA Paper 87-1543, June 1987.

[32]Boyd, I. D., "Monte Carlo Simulation of Nonequilibrium Flow in Low Power Hydrogen Arcjets," *Physics of Fluids*, Vol. 9, 1997, pp. 3086-3095.

American Institute of Aeronautics and Astronautics

Table 1. Baseline forward reaction rate coefficients (m³/molecule/s) used in DPLR.

Number	Reaction	Rate Coefficient
1M	$N_2 + M \Leftrightarrow N + N + M$	1.162×10^{-8} $T^{-1.6}$ exp(-113,200/T)
1A	$N_2 + A \Leftrightarrow N + N + A$	4.980×10^{-8} $T^{-1.6}$ exp(-113,200/T)
1E	$N_2 + E^- \Leftrightarrow N + N + A$	4.980×10^{-6} $T^{-1.6}$ exp(-113,200/T)
2M	$O_2 + M \Leftrightarrow O + O + M$	3.321×10^{-9} $T^{-1.5}$ exp(-59,400/T)
2A	$O_2 + A \Leftrightarrow O + O + A$	1.660×10^{-8} $T^{-1.5}$ exp(-59,400/T)
3M	$NO + M \Leftrightarrow N + O + M$	8.302×10^{-15} exp(-75,500/T)
3A	$NO + A \Leftrightarrow N + O + A$	1.826×10^{-13} exp(-75,500/T)
4	$O + NO \Leftrightarrow N + O_2$	1.389×10^{-17} exp(-19,700/T)
5	$O + N_2 \Leftrightarrow N + NO$	1.069×10^{-12} $T^{-1.000}$ exp(-37,500/T)
6	$N + N \Leftrightarrow N_2^+ + E^-$	3.387×10^{-17} exp(-67,700/T)
7	$O + O \Leftrightarrow O_2^+ + E^-$	1.859×10^{-17} exp(-81,200/T)
8	$N + O \Leftrightarrow NO^+ + E^-$	8.766×10^{-18} exp(-32,000/T)
9	$N + E^- \Leftrightarrow N^+ + 2E^-$	4.151×10^{4} $T^{-3.82}$ exp(-168,600/T)
10	$O + E^- \Leftrightarrow O^+ + 2E^-$	6.475×10^{3} $T^{-3.78}$ exp(-158,500/T)
11	$N_2 + O^+ \Leftrightarrow O + N_2^+$	1.511×10^{-18} $T^{0.360}$ exp(-22,800/T)
12	$NO + O^+ \Leftrightarrow O_2 + N^+$	2.324×10^{-25} $T^{1.900}$ exp(-15,300/T)
13	$O_2 + NO^+ \Leftrightarrow NO + O_2^+$	3.985×10^{-17} $T^{0.410}$ exp(-32,600/T)
14	$N + NO^+ \Leftrightarrow O + N_2^+$	1.195×10^{-16} exp(-35,500/T)
15	$O + NO^+ \Leftrightarrow O_2 + N^+$	1.660×10^{-18} $T^{0.500}$ exp(-77,200/T)
16	$N + O_2^+ \Leftrightarrow O_2 + N^+$	1.444×10^{-16} $T^{0.140}$ exp(-28,600/T)
17	$N_2 + O_2^+ \Leftrightarrow O_2 + N_2^+$	1.644×10^{-17} exp(-40,700/T)
18	$N + NO^+ \Leftrightarrow N_2 + O^+$	5.645×10^{-17} $T^{-1.080}$ exp(-12,800/T)
19	$O + NO^+ \Leftrightarrow N + O_2^+$	1.195×10^{-17} $T^{0.290}$ exp(-48,600/T)

American Institute of Aeronautics and Astronautics

Table 2. Reaction rate coefficients (m^3/molecule/s) used in DSMC.

| Number	Reaction	Rate Coefficient
1M	$N_2 + M \rightarrow N + N + M$	$1.162 \times 10^{-8}\ T^{-1.6}\ \exp(-113{,}200/T)$
1A	$N_2 + A \rightarrow N + N + A$	$4.980 \times 10^{-8}\ T^{-1.6}\ \exp(-113{,}200/T)$
1E	$N_2 + E^- \rightarrow N + N + A$	$4.980 \times 10^{-6}\ T^{-1.6}\ \exp(-113{,}200/T)$
2M	$O_2 + M \rightarrow O + O + M$	$3.321 \times 10^{-9}\ T^{-1.5}\ \exp(-59{,}400/T)$
2A	$O_2 + A \rightarrow O + O + A$	$1.660 \times 10^{-8}\ T^{-1.5}\ \exp(-59{,}400/T)$
3M	$NO + M \rightarrow N + O + M$	$8.302 \times 10^{-15}\ \exp(-75{,}500/T)$
3A	$NO + A \rightarrow N + O + A$	$1.826 \times 10^{-13}\ \exp(-75{,}500/T)$
4F	$O + NO \rightarrow N + O_2$	$1.389 \times 10^{-17}\ \exp(-19{,}700/T)$
4B	$N + O_2 \rightarrow O + NO$	$4.601 \times 10^{-15}\ T^{-0.546}$
5F	$O + N_2 \rightarrow N + NO$	$1.069 \times 10^{-12}\ T^{-1.000}\ \exp(-37{,}500/T)$
5B	$N + NO \rightarrow O + N_2$	$4.059 \times 10^{-12}\ T^{-1.359}$
6F	$N + N \rightarrow N_2^+ + E^-$	$3.387 \times 10^{-17}\ \exp(-67{,}700/T)$
6B	$N_2^+ + E^- \rightarrow N + N$	$7.274 \times 10^{-12}\ T^{-0.650}$
7F	$O + O \rightarrow O_2^+ + E^-$	$1.859 \times 10^{-17}\ \exp(-81{,}200/T)$
7B	$O_2^+ + E^- \rightarrow O + O$	$1.453 \times 10^{-4}\ T^{-2.412}$
8F	$N + O \rightarrow NO^+ + E^-$	$8.766 \times 10^{-18}\ \exp(-32{,}000/T)$
8B	$NO^+ + E^- \rightarrow N + O$	$1.321 \times 10^{-9}\ T^{-1.187}$
9	$N + E^- \rightarrow N^+ + 2E^-$	$8.434 \times 10^{-14}\ \exp(-121{,}000/T)$
10	$O + E^- \rightarrow O^+ + 2E^-$	$1.054 \times 10^{-14}\ \exp(-106{,}200/T)$
11F	$N_2 + O^+ \rightarrow O + N_2^+$	$1.511 \times 10^{-18}\ T^{0.360}\ \exp(-22{,}800/T)$
11B	$O + N_2^+ \rightarrow N_2 + O^+$	$1.978 \times 10^{-18}\ T^{0.109}$
12F	$NO + O^+ \rightarrow O_2 + N^+$	$2.324 \times 10^{-25}\ T^{1.900}\ \exp(-15{,}300/T)$
12B	$O_2 + N^+ \rightarrow NO + O^+$	$2.443 \times 10^{-26}\ T^{2.102}$
13F	$O_2 + NO^+ \rightarrow NO + O_2^+$	$3.985 \times 10^{-17}\ T^{0.410}\ \exp(-32{,}600/T)$
13B	$NO + O_2^+ \rightarrow O_2 + NO^+$	$6.195 \times 10^{-16}\ T^{-0.050}$
14F	$N + NO^+ \rightarrow O + N_2^+$	$1.195 \times 10^{-16}\ \exp(-35{,}500/T)$
14B	$O + N_2^+ \rightarrow N + NO^+$	$1.744 \times 10^{-18}\ T^{0.302}$
15F	$O + NO^+ \rightarrow O_2 + N^+$	$1.660 \times 10^{-18}\ T^{0.500}\ \exp(-77{,}200/T)$
15B	$O_2 + N^+ \rightarrow O + NO^+$	$2.192 \times 10^{-17}\ T^{0.114}$
16F	$N + O_2^+ \rightarrow O_2 + N^+$	$1.444 \times 10^{-16}\ T^{0.140}\ \exp(-28{,}600/T)$
16B	$O_2 + N^+ \rightarrow N + O_2^+$	$4.993 \times 10^{-18}\ T^{-0.004}$
17F	$N_2 + O_2^+ \rightarrow O_2 + N_2^+$	$1.644 \times 10^{-17}\ \exp(-40{,}700/T)$
17B	$O_2 + N_2^+ \rightarrow N_2 + O_2^+$	$4.589 \times 10^{-18}\ T^{-0.037}$
18F	$N + NO^+ \rightarrow N_2 + O^+$	$5.645 \times 10^{-17}\ T^{-1.080}\ \exp(-12{,}800/T)$
18B	$N_2 + O^+ \rightarrow N + NO^+$	$3.970 \times 10^{-18}\ T^{-0.710}$
19F	$O + NO^+ \rightarrow N + O_2^+$	$1.195 \times 10^{-17}\ T^{0.290}\ \exp(-48{,}600/T)$
19B	$N + O_2^+ \rightarrow O + NO^+$	$8.918 \times 10^{-13}\ T^{-0.969}$
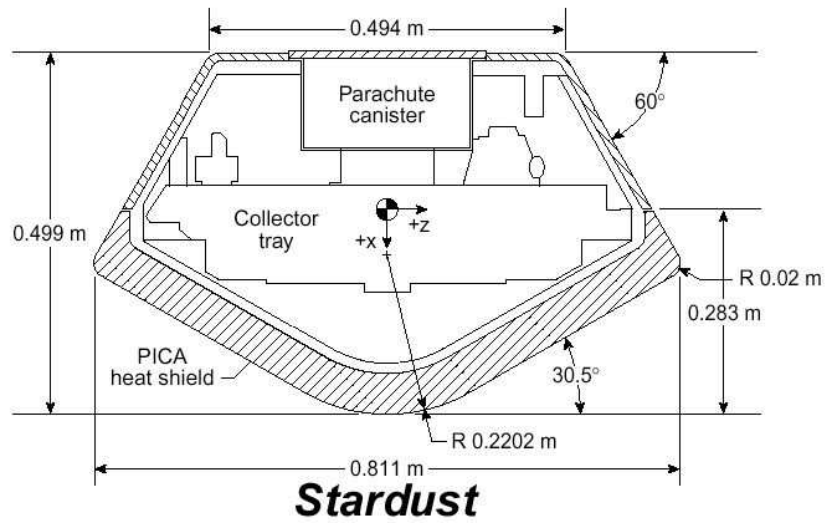
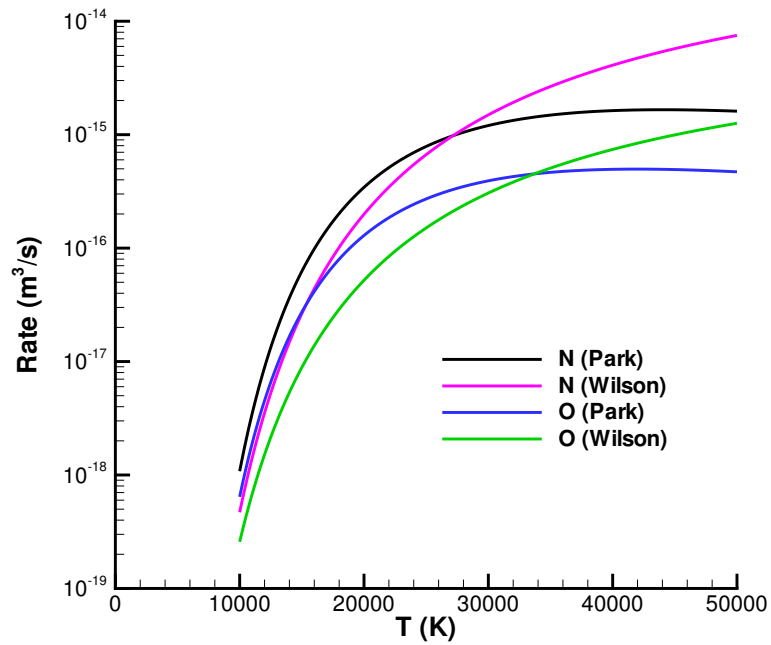Figure 1. Geometry of the Stardust Return Capsule.

Figure 2. Direct ionization rates of atomic nitrogen and oxygen as a function of temperature.
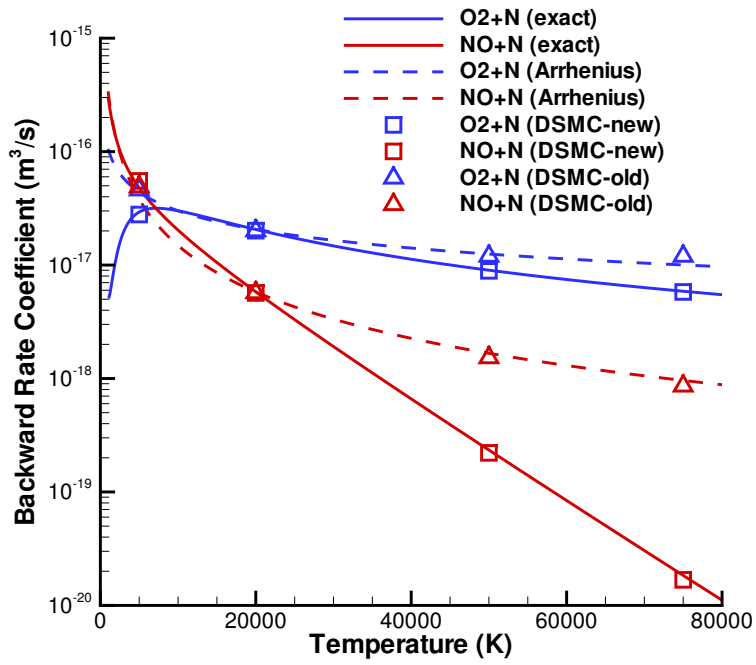
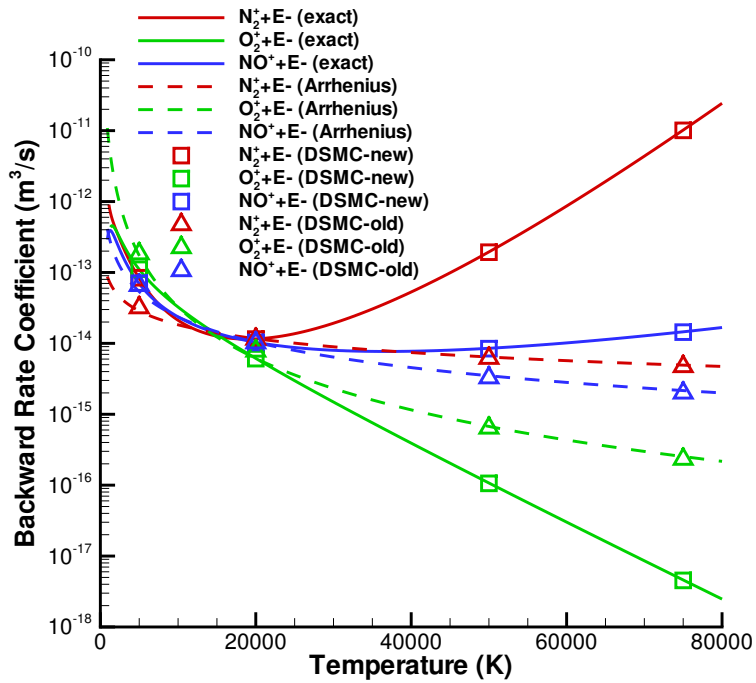**Figure 3.** Backward reaction rates for the Zeldovich exchange reactions as a function of temperature.

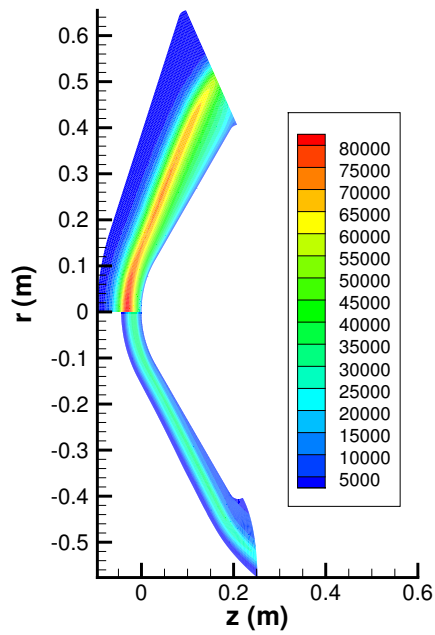**Figure 4.** Backward reaction rates for associative ionization as a function of temperature.

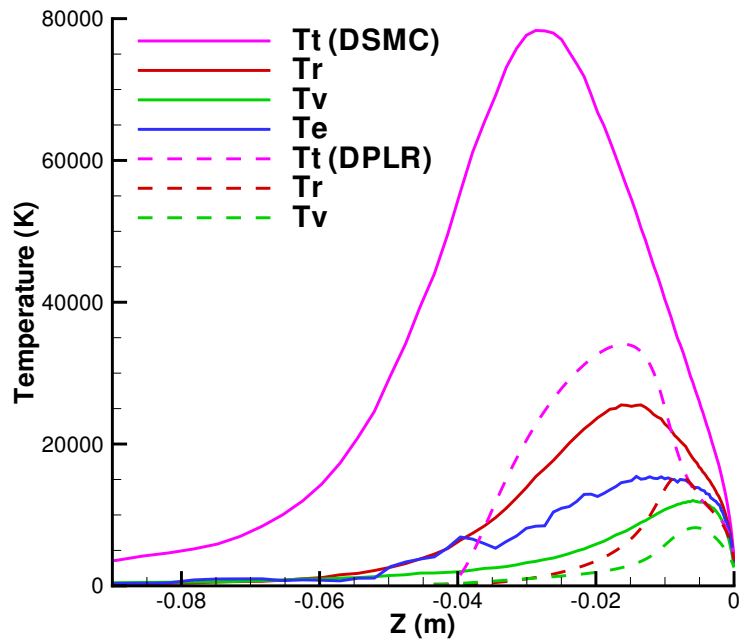**Figure 5.** Contours of translational temperature (K) for the Stardust Return Capsule at 81 km obtained using DSMC (upper) and DPLR (lower).

Figure 6. Profiles of temperature along the stagnation streamline for the Stardust Return Capsule at 81 km.

American Institute of Aeronautics and Astronautics
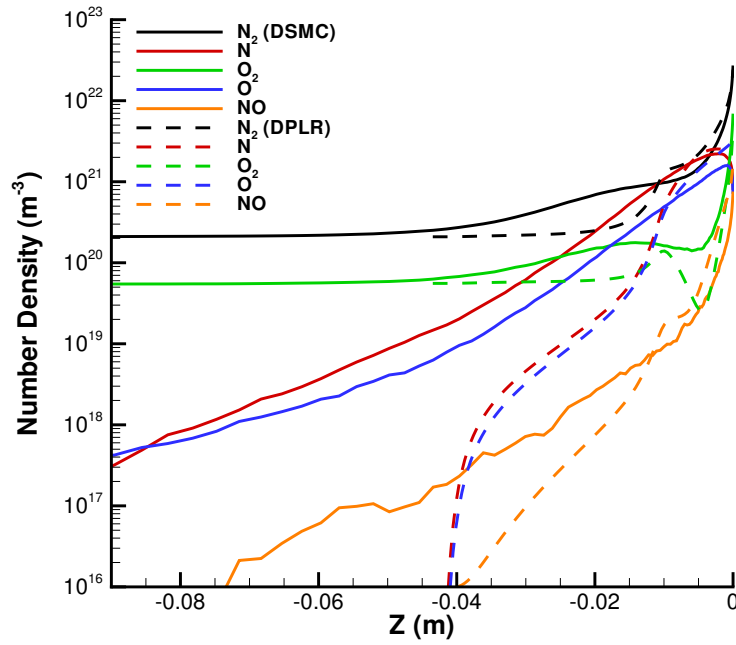
Figure 7. Profiles of neutral species number density along the stagnation streamline for the Stardust Return Capsule at 81 km.
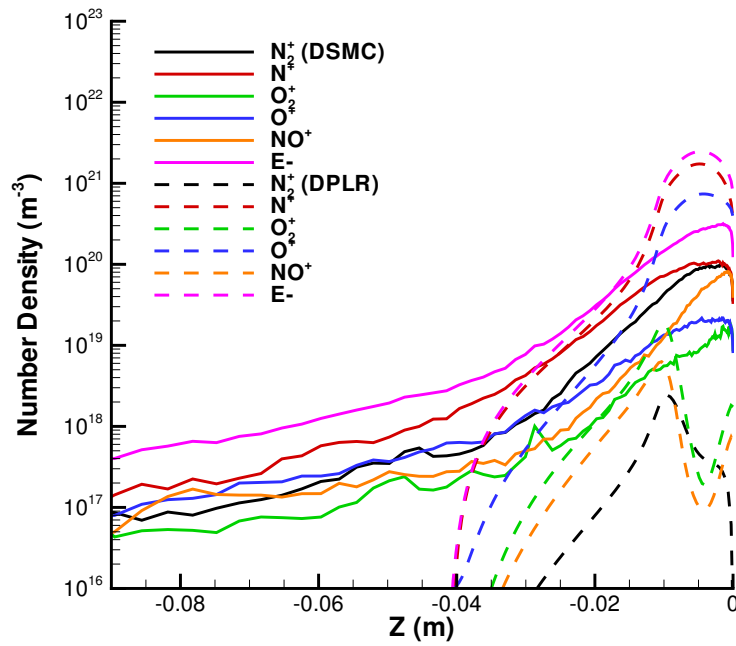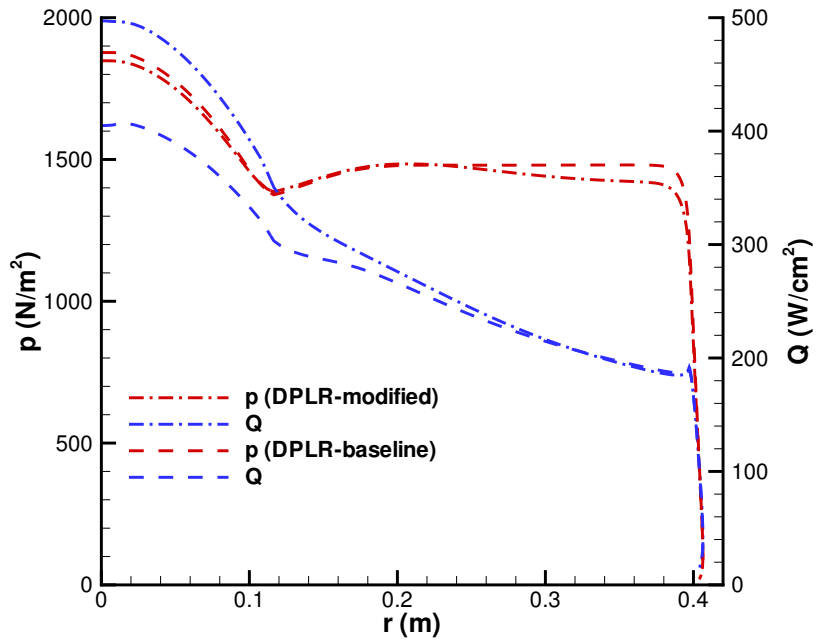

Figure 8. Profiles of charged species number density along the stagnation streamline for the Stardust Return Capsule at 81 km.
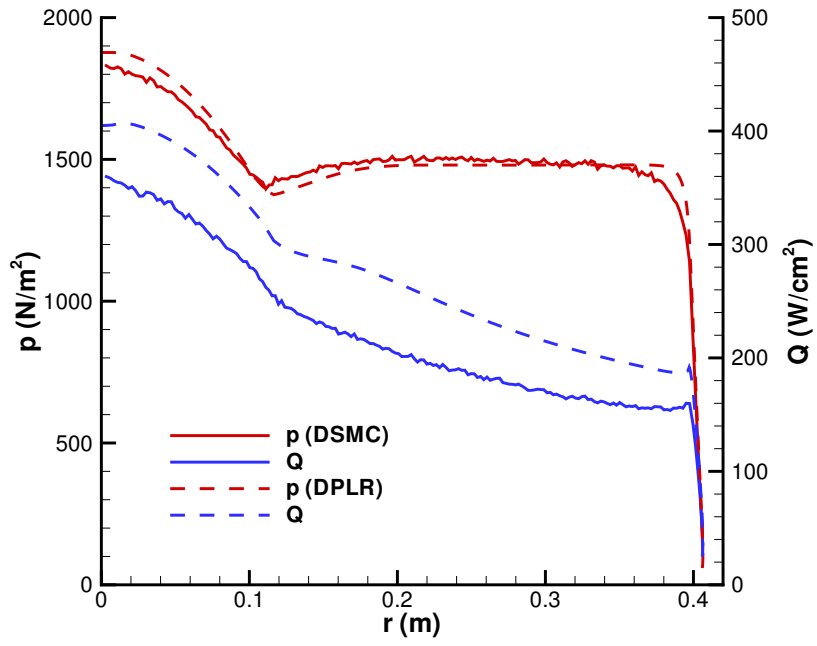
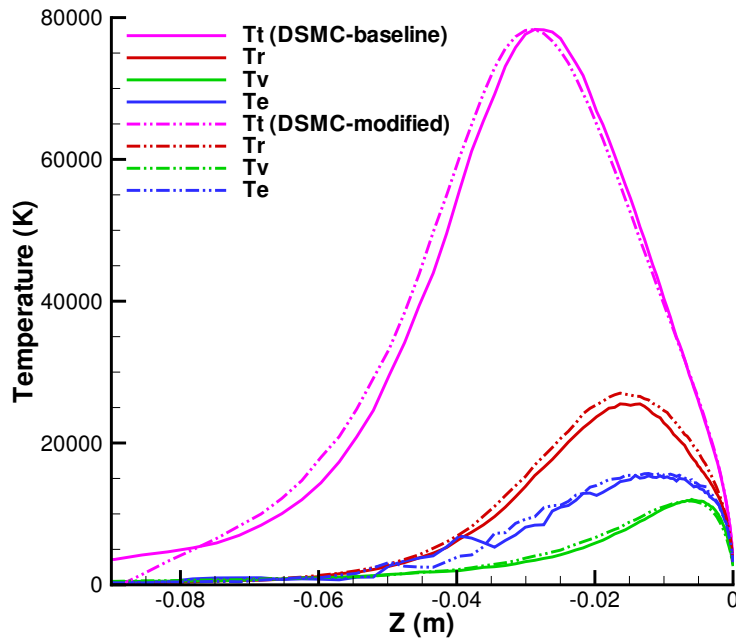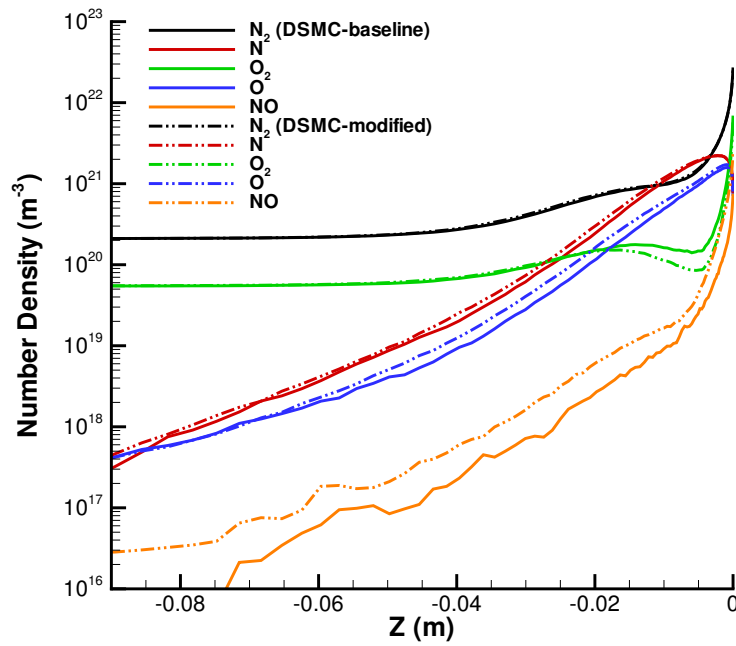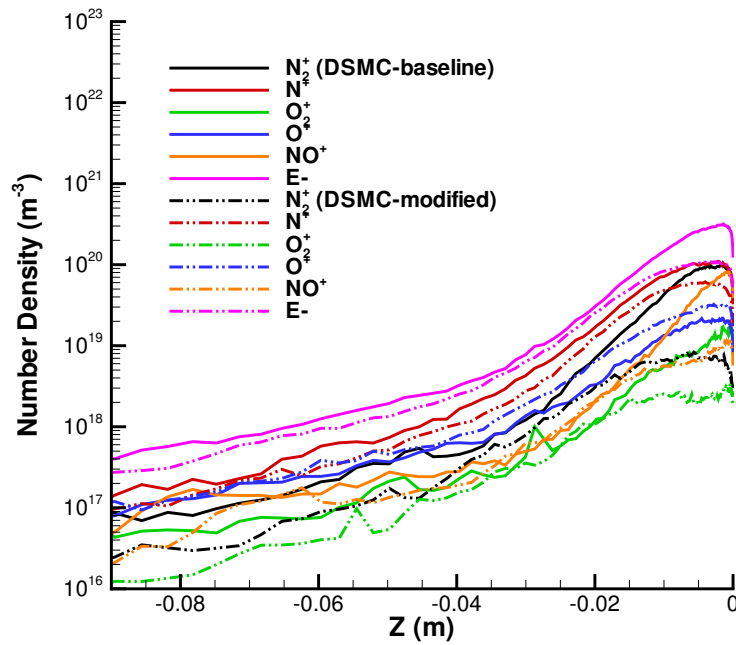Figure 9. Profiles of pressure and heat flux along the surface of the Stardust Return Capsule at 81 km.
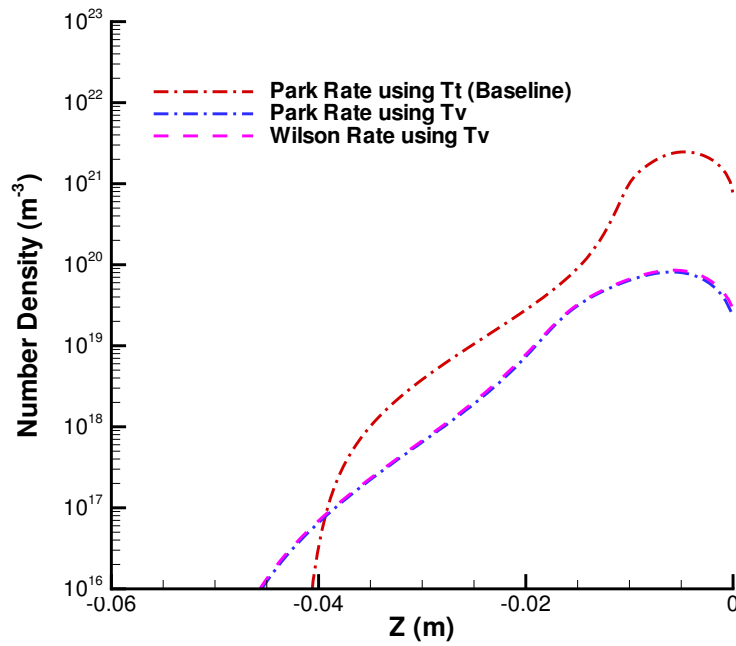
Figure 10. Profiles of electron number density along the stagnation streamline for the Stardust Return Capsule at 81 km.

American Institute of Aeronautics and Astronautics
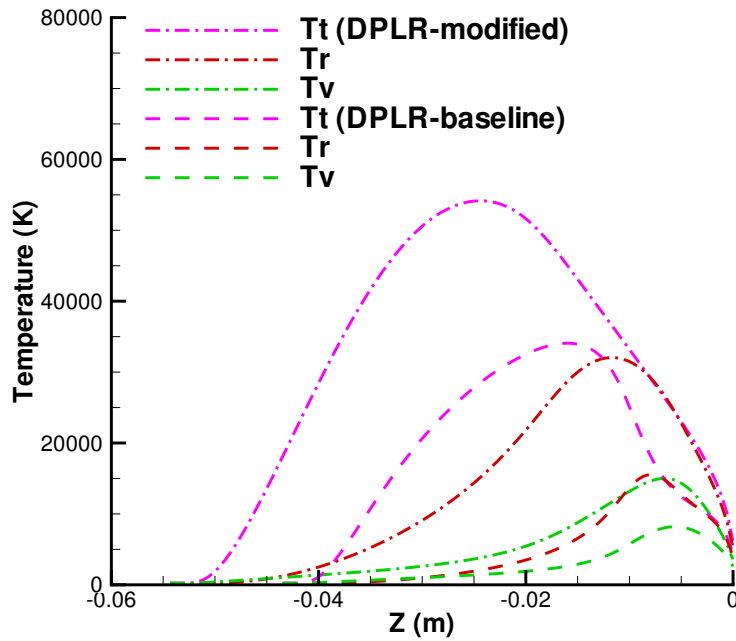
Figure 11. Profiles of temperature along the stagnation streamline for the Stardust Return Capsule at 81 km.
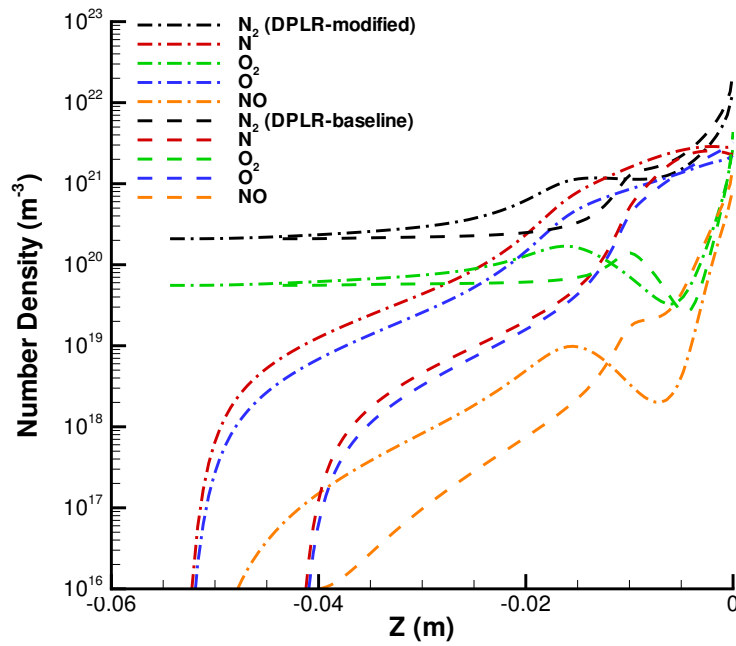
Figure 12. Profiles of neutral species number density along the stagnation streamline for the Stardust Return Capsule at 81 km.
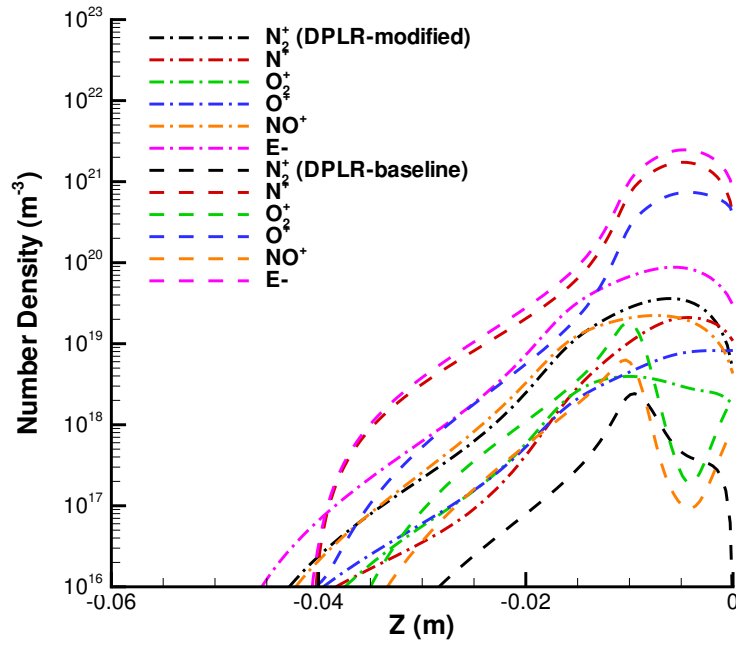
Figure 13. Profiles of charged species number density along the stagnation streamline for the Stardust Return Capsule at 81 km.
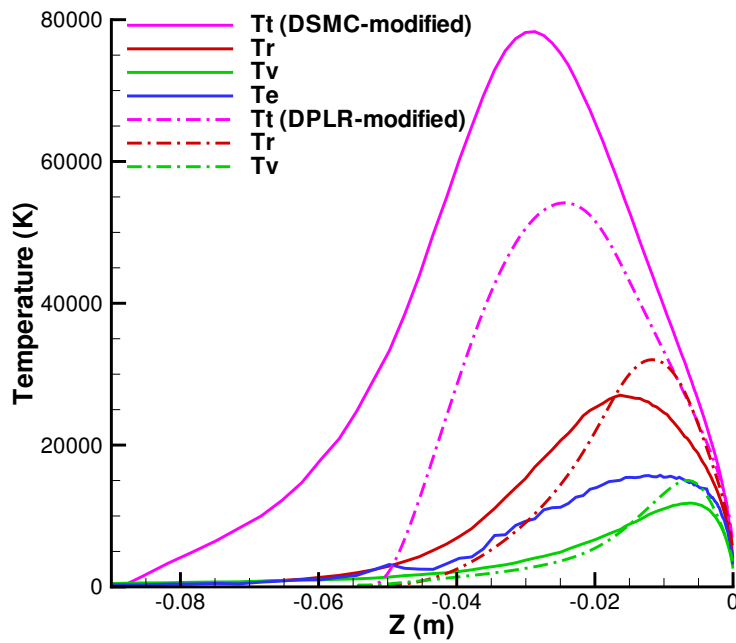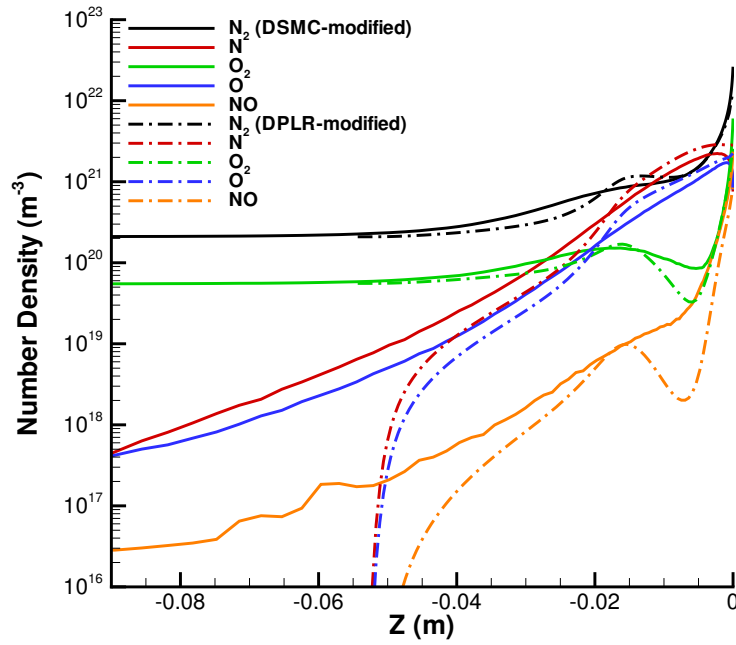

Figure 14. Profiles of pressure and heat flux along the surface of the Stardust Return Capsule at 81 km.

American Institute of Aeronautics and Astronautics

Figure 15. Profiles of temperature along the stagnation streamline for the Stardust Return Capsule at 81 km.

Figure 16. Profiles of neutral species number density along the stagnation streamline for the Stardust Return Capsule at 81 km.
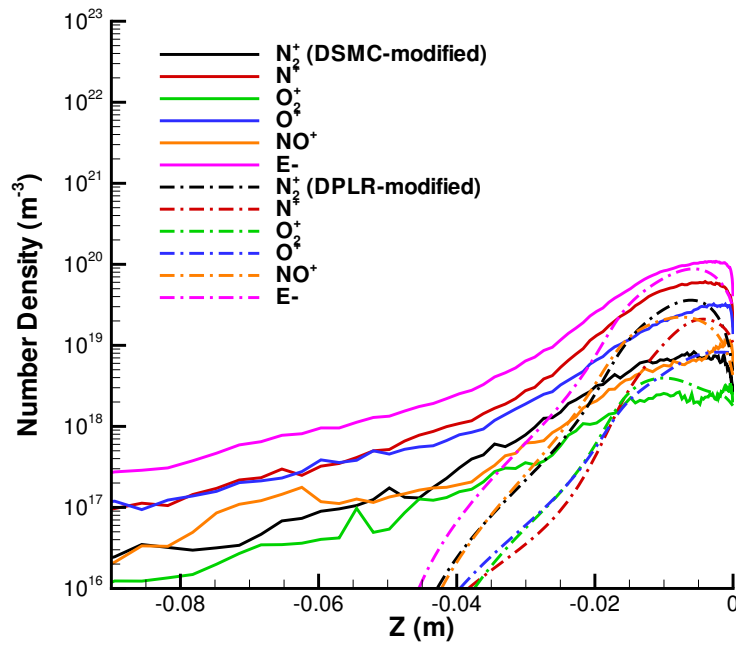
Figure 17. Profiles of charged species number density along the stagnation streamline for the Stardust Return Capsule at 81 km.

Figure 18. Profiles of temperature along the stagnation streamline for the Stardust Return Capsule at 81 km.

American Institute of Aeronautics and Astronautics

Figure 19. Profiles of neutral species number density along the stagnation streamline for the Stardust Return Capsule at 81 km.

Figure 20. Profiles of charged species number density along the stagnation streamline for the Stardust Return Capsule at 81 km.
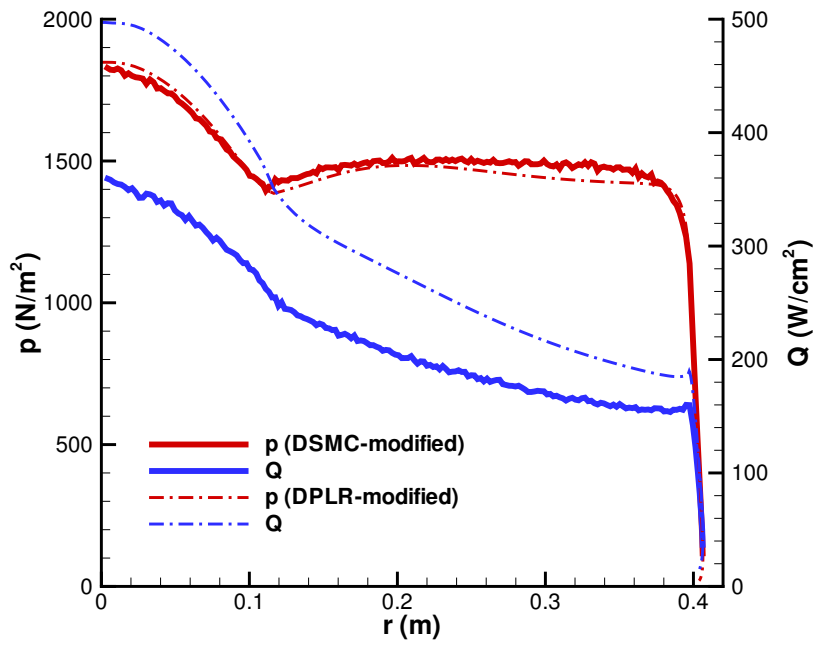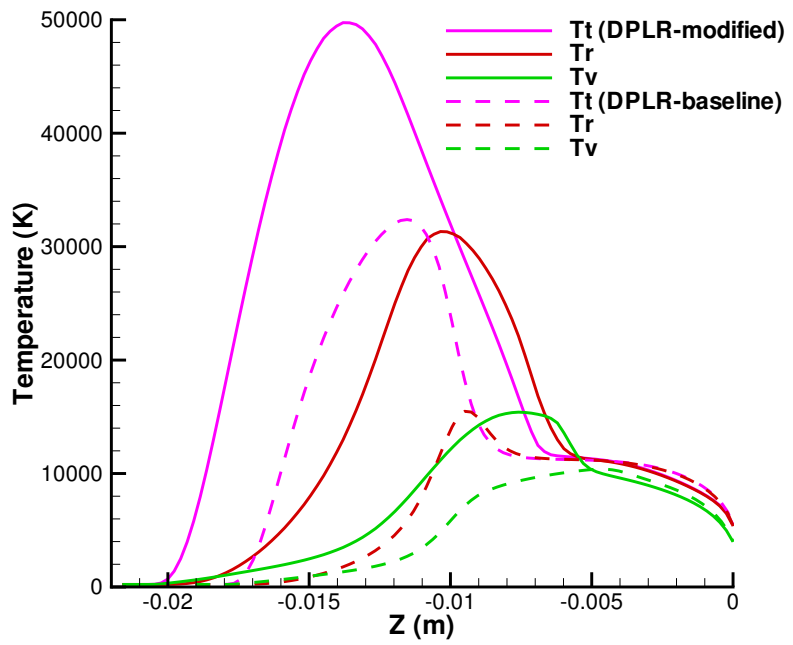
American Institute of Aeronautics and Astronautics

Figure 21. Profiles of pressure and heat flux along the surface of the Stardust Return Capsule at 81 km.

Figure 22. Profiles of temperature along the stagnation streamline for the Stardust Return Capsule at 71 km.
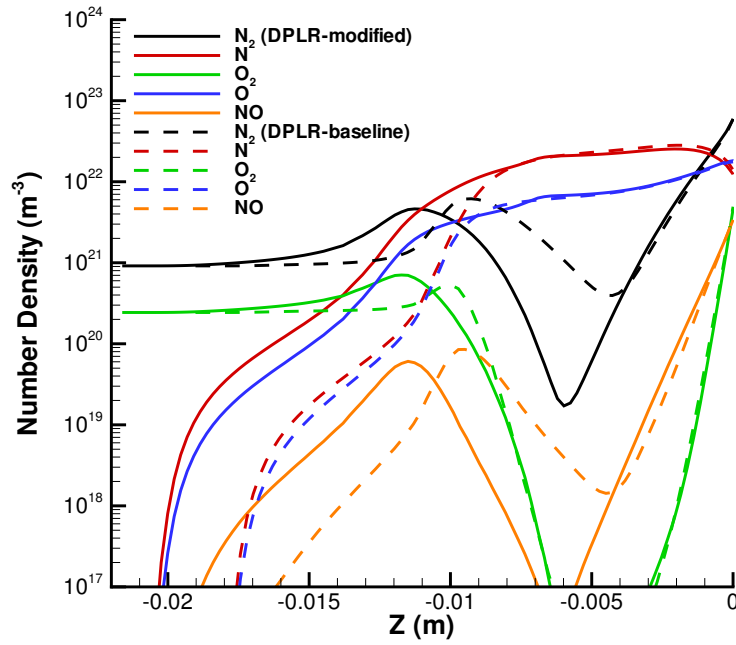
American Institute of Aeronautics and Astronautics

Figure 23. Profiles of neutral species number density along the stagnation streamline for the Stardust Return Capsule at 71 km.

Figure 24. Profiles of charged species number density along the stagnation streamline for the Stardust Return Capsule at 71 km.
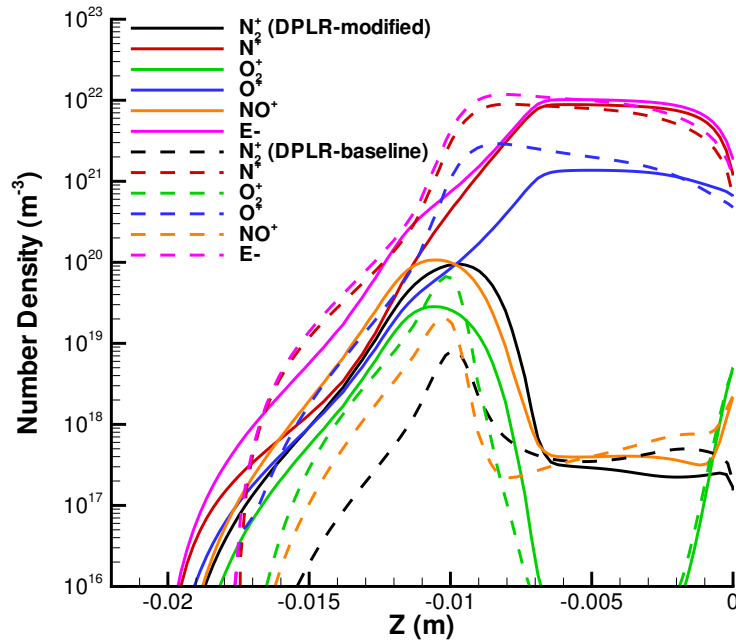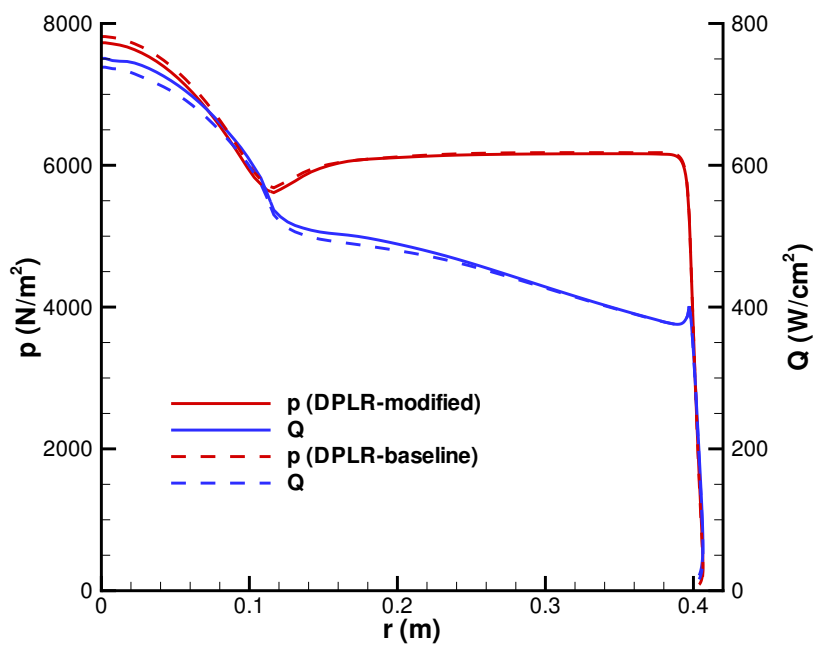
American Institute of Aeronautics and Astronautics

Figure 25. Profiles of pressure and heat flux along the surface of the Stardust Return Capsule at 71 km.